Ultrasonic Imaging in Highly Attenuating Materials With Hadamard Codes and the Decomposition of the Time Reversal Operator

Eduardo Lopez Villaverde, Sébastien Robert, and Claire Prada

***Abstract*— In this paper, defects in a high density polyethylene pipe are imaged with the total focusing method. The viscoelastic attenuation of this material greatly reduces the signal level and leads to a poor signal-to-noise ratio (SNR) due to electronic noise. To improve the image quality, the decomposition of the time reversal operator method is combined with the spatial Hadamard coded transmissions before calculating images in the time domain. Because the Hadamard coding is not compatible with conventional imaging systems, this paper proposes two modified coding methods based on sparse Hadamard matrices with +1/0 coefficients. The SNRs expected with the different spatial codes are demonstrated, and then validated on both simulated and experimental data. Experiments are performed with a transducer array in contact with the base material of a polyethylene pipe. In order to improve the noise filtering procedure, the singular values associated with electronic noise are expressed on the basis of the random matrix theory. This model of noise singular values allows a better identification of the defect response in noisy experimental data. Finally, the imaging method is evaluated in a more industrial inspection configuration, where an immersion array probe is used to image defects in a butt fusion weld with a complex geometry.**

***Index Terms*— Attenuating material, defect characterization, nondestructive evaluation (NDE), time reversal, ultrasonic array imaging.**

I. Introduction

THIS paper presents a theoretical and experimental study that aims to improve ultrasonic array imaging of high density polyethylene (HDPE) pipes. This material has been used in place of steel alloys in different industries (petrochemical, power generation, mining, and so on) due to its notable resistance to corrosion and erosion [1]. In comparison with usual metallic welds, the HDPE fusion joints can be considered as homogeneous and isotropic but the high viscoelastic attenuation of the material [2] makes the weld inspection difficult. This attenuation may reduce the signal amplitude to a level close or even lower than the electronic noise introduced by the signal acquisition system.

Manuscript received January 6, 2017; accepted March 30, 2017. Date of publication April 3, 2017; date of current version August 28, 2017. *(Corresponding author: Sébastien Robert.)*

E. Lopez Villaverde and S. Robert are with the Laboratory for Integration of Systems and Technology, Commissariat à l´Énergie Atomique et aux Énergies Alternatives, Department of Imaging and Simulation for Nondestructive Testing, F-91191 Gif-sur-Yvette, France (e-mail: eduardo.lopezvillaverde@cea.fr; sebastien.robert@cea.fr)

C. Prada is with the Centre National de la Recherche Scientifique, Institut Langevin, École Supérieure de Physique Et de Chimie Industrielles de la Ville De Paris, PSL Research University, 75005 Paris, France (e-mail: claire.prada-julia@espci.fr).

Digital Object Identifier 10.1109/TUFFC.2017.2690499

Rather than imaging the HDPE material with a delay-and-sum beamforming based on the transmission of focused waves [3], a more interesting alternative is represented by the synthetic transmit aperture [4], better known as a total focusing method (TFM) in nondestructive evaluation (NDE) [5]. The TFM is a synthetic focusing in transmit and receive modes at every pixel of an image, which provides excellent contrast and resolution everywhere in the region of interest. Another advantage of TFM is that the focusing algorithm is applied to a set of signals that represents the interelement impulse response matrix of the medium. This offers the possibility of reducing the noise with advanced spatiotemporal filtering methods, such as the decomposition of the time reversal operator (DORT) method [6]. For instance, in a previous study where defects were detected in coarse grained stainless steels of the nuclear industry, it was demonstrated that a significant part of the structural noise can be removed from the signals with the DORT method, and the filtering operation remains compatible with the TFM imaging in the time domain [7].

For the TFM imaging combined with DORT to remain fully efficient in polyethylene, it is necessary to optimize the array response matrix acquisition. In the conventional acquisition where the array elements are excited one by one with identical short electric pulses, the amplitude of the wave transmitted by a single element rapidly decreases due to the cylindrical spreading losses and the strong viscoelastic attenuation. In order to overcome this problem, two main approaches are studied in the literature. In the first one, the elements are excited individually with long-duration signals, such as chirp signals [8] or Golay codes [9]. However, the Golay temporal coding is not compatible with the electronic design of most of the imaging systems, where the same electric pulse is sent to the channels. Furthermore, specifically in NDE, images frequently display saturated echoes (e.g., echoes of the surface or the back wall of a steel specimen), and excitations with long-duration signals extend the saturation areas in the region of interest, which can potentially mask a defect echo.

In the second approach, some or all elements are excited in parallel with short electric pulses. The principle of virtual sources was extensively studied in medical imaging in the 1990s [10], and more recently in NDE [11]. The principle is to fire a few adjacent elements with appropriate delays in order to transmit the same diverging wave as a single element, but with a higher acoustic power. In strongly attenuating media, the contribution of virtual sources is quite limited, because

the amplitude of incident waves is increased by a factor of $1.25\sqrt{n}$, where the number n of adjacent transmitters to create a virtual source is much smaller than the number N of array elements. A more efficient way to increase the acoustic energy sent into the medium consists in exciting simultaneously the N elements with Hadamard spatial codes [12]. Signals are recorded by emitting N waves with the full array and, for every wave transmission, the N electric signals applied to the N elements are multiplied by a combination of $+1/-1$ coefficients. From the N^2 collected signals, an equivalent impulse response matrix is obtained with a decoding operation. The Hadamard coded excitations increase the signal-to-noise ratio (SNR) by a factor of $\sqrt{N}$ compared with a conventional acquisition of the impulse response matrix [13].

To enhance the quality of images in polyethylene pipes, we propose to associate the Hadamard coded excitations with the DORT method. The coded excitations increase the penetration depth of ultrasounds in the material, and the DORT method is used to remove the electronic noise from data. The combination of coded transmissions with DORT is an approach proposed by Lingevitch *et al.* [14] in underwater acoustics and also used by Nauleau *et al.* [15] for detection and characterization in the medical field. In imaging with TFM, this combination of methods requires two additional steps: the decoding operation to obtain the impulse response matrix of the medium, and the postprocessing of this matrix with the imaging equation in the time domain. This paper also proposes two modified Hadamard coding methods that are compatible with conventional imaging systems. Both methods are based on $+1/0$ coefficients, which mean that a part of the array elements are excited with the same pulse, while all the others are disabled. The noise filtering with the DORT method is performed in the frequency domain. Next, by inverse Fourier transforms, the free-noise TFM images are calculated in the time domain. The noise filtering procedure consists in the identification of the singular values of the transfer matrix that are associated with noise. To this end, the theoretical distribution of noise singular values is established with the random matrix theory [16].

This paper is organized as follows. Section II describes the overall principle of the imaging method that comprises three main steps: 1) acquisition of the impulse response matrix with the Hadamard coded excitations; 2) noise elimination with the DORT method; and 3) image formation with TFM. Section III presents two modified spatial coding methods for usual imaging systems. The SNRs expected with the different coding methods are demonstrated, and then validated on both simulated and experimental data. Section IV is devoted to the analysis of the singular values of the transfer matrix. The theoretical decreasing law of the singular values associated with noise is established in order to identify the defect response in noisy data. In Section V, the imaging method is evaluated experimentally with the images of artificial defects in the butt fusion weld of an HDPE sample.

II. General Principle of the Method

The imaging method consists in three steps: the acquisition of the impulse response matrix, the matrix filtering using the DORT method, and the image calculation by numerical focusing in transmit and receive modes (TFM). The different steps are summarized hereafter.

A. Data Acquisition With Hadamard Spatial Coding

The TFM is a beamforming algorithm commonly applied to the impulse response matrix $\mathbf{K}(t)$. For an array of N elements, $\mathbf{K}(t)$ is a symmetric matrix composed of the N^2 interelement impulse responses of the array. A component $K_{nm}(t)$ of this matrix represents the signal recorded with the element n when the element m is excited with an electric pulse. In high attenuating viscoelastic media, this data acquisition principle (elements excited one by one) may lead to a poor SNR because of the spreading losses and the low amplitude of the transmitted waves. The simultaneous excitation of all the array elements with orthogonal Walsh–Hadamard codes improves the SNR in the data. The spatial coding for the mth transmission corresponds to the coefficients of the mth column of the Hadamard matrix $\mathbf{H}_N$ of order N. This matrix is symmetric and verifies $\mathbf{H}_N\mathbf{H}_N^t = N\mathbf{I}_N$ [17]. It is only composed of $+1/-1$ coefficients. Following Sylvester's construction, it can be recursively defined as:

$$\mathbf{H}_{2^k} = \begin{pmatrix} +\mathbf{H}_{2^{k-1}} & +\mathbf{H}_{2^{k-1}} \\ +\mathbf{H}_{2^{k-1}} & -\mathbf{H}_{2^{k-1}} \end{pmatrix} \tag{1}$$

for $k \in \mathbb{N}^*$, with the first-order Hadamard matrix $\mathbf{H}_1 = (+1)$. From the acquisition matrix $\mathbf{W}(t)$ obtained by applying the Walsh–Hadamard coded excitations, an equivalent impulse response matrix $\mathbf{K}^H(t)$ can be calculated using the following decoding operation:

$$\mathbf{K}^H(t) = \frac{1}{N}\mathbf{W}(t)\mathbf{H}_N. \tag{2}$$

In the presence of uncorrelated electronic noise, it is shown in [13] that the SNR (in dB) of the signals contained in $\mathbf{K}^H(t)$ is improved by $10\log_{10}(N)$ compared with those in $\mathbf{K}(t)$.

B. Decomposition of the Time Reversal Operator

In order to filter the noise as much as possible, a singular value decomposition (SVD) of the transfer matrix $\hat{\mathbf{K}}^H(f)$ is calculated at each frequency f in the array bandwidth. This matrix is defined as the Fourier transform of $\mathbf{K}^H(t)$ and can be written as the sum of two matrices

$$\hat{\mathbf{K}}^H(f) = \hat{\mathbf{K}}_s^H(f) + \boldsymbol{\eta}(f) \tag{3}$$

where $\boldsymbol{\eta}(f)$ is the noise matrix, and $\hat{\mathbf{K}}_s^H(f)$ is the signal matrix. If $P(f)$ is the number of large singular values associated with defects, $\hat{\mathbf{K}}_s^H(f)$ is defined by

$$\hat{\mathbf{K}}_s^H(f) = \sum_{p=1}^{P(f)} \lambda_p(f)\mathbf{u}_p(f)\mathbf{v}_p^\dagger(f). \tag{4}$$

For point-like and well-resolved reflectors, $P(f)$ is the number of defects that are detected at the frequency f, and $\lambda_p(f)$ is the pth singular value characterizing the reflectivity of one of the defects. The transmission and reception singular vectors, $\mathbf{v}_p(f)$ and $\mathbf{u}_p(f)$, describe the wave propagation from the

array to the defect, and from the defect to the array. If the dimension $P(f)$ of the signal subspace is determined for each frequency, $\hat{\mathbf{K}}_s^H(f)$ thus contains only information about the defects, and the time-domain TFM algorithm applied to the impulse response matrix $\mathbf{K}_s^H(t)$ provides a high contrast image.

C. Image Formation With the Total Focusing Method

The TFM imaging is equivalent to a dynamic focusing in transmit and receive modes at every point of a region of interest. If $K_{nm}(t)$ denotes the interelement signals contained in $\mathbf{K}_s^H(t)$, the focusing algorithm consists in a coherent sum of the N^2 analytic signals $S_{nm}(t) = K_{nm}(t) + j\mathcal{H}[K_{nm}(t)]$, where $\mathcal{H}$ denotes the Hilbert transform. With the notations defined in Fig. 1, the general form of the TFM imaging equation is

$$I(\mathbf{r}) = \left| \sum_{m=1}^{N} \sum_{n=1}^{N} \mu_m(\mathbf{r}) \nu_n(\mathbf{r}) S_{nm}[t_{nm}(\mathbf{r})] \right| \tag{5}$$

where $\mathbf{r}$ is the position vector of a given focusing point $M(\mathbf{r})$; $t_{nm}(\mathbf{r})$ is the theoretical interelement propagation time from transmitter m to receiver n for a focusing point at $\mathbf{r}$

$$t_{nm}(\mathbf{r}) = \frac{\|\mathbf{r} - \mathbf{r}_m\|}{c} + \frac{\|\mathbf{r} - \mathbf{r}_n\|}{c} \tag{6}$$

and c is the velocity of the longitudinal waves in the medium. The weighting factors $\mu_m(\mathbf{r})$ and $\nu_n(\mathbf{r})$ are introduced to filter imaging artifacts (caused by aliasing, aperture edge diffraction effects, geometry echoes, and so on) [18], or to compensate losses due to the element beam pattern and the cylindrical spreading. In this paper, the apodization factors are intended to correct losses related to the limited divergence of the diffracted beams in polyethylene. They are identical in transmission and reception [i.e., $\mu_m(\mathbf{r}) = \nu_m(\mathbf{r})$] and are set equal to $1/D_m(\mathbf{r})$, where $D_m(\mathbf{r})$ is the directivity function of an array element radiating in a fluid medium [19]

$$D_m(\mathbf{r}) = \sin c\left(\frac{a\pi f_c}{c} \sin\theta_m(\mathbf{r})\right) \cos\theta_m(\mathbf{r}) \tag{7}$$

where a is the element width, f_c is the mean center frequency of the N elements, and $\theta_m(\mathbf{r})$ is the radiation angle in the direction of $M(\mathbf{r})$ for the element m. It is defined as $\theta_m(\mathbf{r}) = \sin^{-1}((\mathbf{r} - \mathbf{r}_m).\mathbf{n}_x / \|\mathbf{r} - \mathbf{r}_m\|)$, where $\mathbf{n}_x = (1\ 0)^t$ is the unit vector in the x-direction.

It should be pointed out that the more exact directivity function in solids [20] is not used because the phase velocity of transverse waves is difficult to measure in polyethylene and these waves can be neglected for imaging because of their very high attenuation [21]. The second observation is that $\mathbf{K}_s^H(t)$ is a symmetric matrix due to the reciprocity principle. This property is not taken into account in (5) to reduce computation times [22], because this would complicate the noise analysis proposed hereafter. In addition, the reciprocity principle reduces the SNR in the presence of electronic noise.

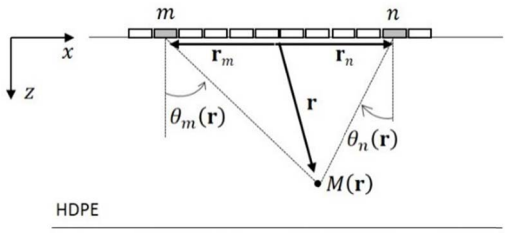

Fig. 1. Contact testing configuration for imaging in the HDPE base material. Two-dimensional imaging geometry and notations used in the TFM equation.

III. Modified Hadamard Spatial Coding

As most imaging electronic devices apply identical electric signals to all channels, two modified acquisitions of the impulse response matrix with the Hadamard basis are proposed hereafter. Then, the SNRs obtained using these modified coded excitations are analyzed.

A. Spatial Coding With Sparse Hadamard Matrices

The optimal coding based on $+1/-1$ excitation coefficients is not compatible with most of the imaging systems, because the same electric signal is sent to all channels. In medical imaging, some authors proposed alternatives to avoid this inconvenient, such as the S-sequence [23] where the spatial coding is based on a binary code $+1/0$, or the delayed encoded excitations [24] which needs a decoding operation in the frequency domain before imaging. In this paper, we present two solutions giving an equivalent set of signals as that obtained with the theoretical $+1/-1$ Hadamard coding. The first solution is to perform two data acquisitions [25] with two sparse matrices, $\mathbf{H}_N^+$ and $\mathbf{H}_N^-$, defined as

$$\mathbf{H}_N^{\pm} = \frac{1}{2}(\mathbf{J}_N \pm \mathbf{H}_N) \tag{8}$$

where $\mathbf{J}_N$ is an $N \times N$ matrix of ones. The sparse matrices $\mathbf{H}_N^+$ and $\mathbf{H}_N^-$ are composed of $+1/0$ coefficients, and the associated acquisition matrices, $\mathbf{W}^+(t)$ and $\mathbf{W}^-(t)$, are recorded when the same electric signal is only sent to the array elements associated with $+1$. Then, the equivalent impulse response matrix is obtained with the following decoding operation:

$$\mathbf{K}^{\pm}(t) = \frac{1}{N}[\mathbf{W}^+(t) - \mathbf{W}^-(t)]\mathbf{H}_N. \tag{9}$$

This data acquisition needs to fire $2N - 1$ times (i.e., N transmissions with the columns of $\mathbf{H}_N^+$, and $N - 1$ with those of $\mathbf{H}_N^-$ because the first column of the latter contains only 0), which is a drawback in real-time imaging. Thus, another solution is to collect only the matrix $\mathbf{W}^+(t)$, and to calculate

$$\mathbf{K}^+(t) = \frac{1}{N}[2\mathbf{W}^+(t) - \mathbf{P}^+(t)]\mathbf{H}_N \tag{10}$$

where the N columns of $\mathbf{P}^+(t)$ are equal to the first column of $\mathbf{W}^+(t)$, i.e., $P_{nm}^+(t) = W_{n1}^+(t)$. It should be noted that $P_{nm}^+(t)$ corresponds to the nth received signal when a plane wave is transmitted with the full array, since the first column of $\mathbf{H}_N^+$ is composed of $+1$. This second approach is more advantageous for real-time imaging, because N transmissions are required

instead of $2N-1$, but the SNR will be reduced in return. The choice of the method is thus a tradeoff between image quality and acquisition time or frame rate.

B. Theoretical Signal-to-Noise Ratios

A theoretical study of the noise level was conducted in order to predict the image quality according to the data acquisition procedure. For each spatial coding, the theoretical SNR of the interelement impulse responses can be established by assuming that signals are disturbed by a zero-mean additive noise, denoted by $\eta_{nm}(t)$, and characterized by the variance σ^2. $\eta_{nm}(t)$ is an electronic noise that does not depend on the array excitation method, which means that its statistical properties are identical in the acquisition matrices $\mathbf{K}(t)$, $\mathbf{W}^+(t)$, $\mathbf{W}^-(t)$, and $\mathbf{W}(t)$.

To start with, the spatial coding with the Hadamard matrix $\mathbf{H}_N$ is considered and the noisy signals are written as

$$\tilde{W}_{nm}(t) = W_{nm}(t) + \eta_{nm}(t). \tag{11}$$

Then, according to the decoding operation in (2), the interelement impulse responses are

$$\tilde{K}^H_{nm}(t) = K^H_{nm}(t) + \zeta_{nm}(t) \tag{12}$$

where $\zeta_{nm}(t)$ is a new additive noise

$$\zeta_{nm}(t) = \frac{1}{N}\sum_{p=1}^{N} \eta_{np}(t) H_{pm}. \tag{13}$$

$\zeta_{nm}(t)$ is defined as a linear combination of zero-mean random variables, and therefore, $\langle \zeta_{nm}(t) \rangle = 0$. In addition, as the weighting coefficients H_{pm} in (13) are equal to ± 1, the noise variance

$$\langle |\zeta_{nm}(t)|^2 \rangle = \left\langle \frac{1}{N^2}\sum_{p=1}^{N} \eta^2_{np}(t) H^2_{pm} \right\rangle \tag{14}$$

can be reduced to

$$\langle |\zeta_{nm}(t)|^2 \rangle = \sigma^2/N. \tag{15}$$

Hence, the standard deviation of the noise in the decoded matrix $\tilde{\mathbf{K}}^H(t)$ is theoretically divided by $\sqrt{N}$ compared with that in the acquisition matrix $\tilde{\mathbf{W}}(t)$ and in the impulse response matrix $\tilde{\mathbf{K}}(t)$. On the other hand, as the signal levels are identical in $\tilde{\mathbf{K}}(t)$ and in $\tilde{\mathbf{K}}^H(t)$, it follows that the SNR is multiplied by $\sqrt{N}$ when images are calculated with $\tilde{\mathbf{K}}^H(t)$.

For the second coding using the two excitation matrices $\mathbf{H}^+_N$ and $\mathbf{H}^-_N$, the signals contained in $\tilde{\mathbf{W}}^+(t)$ and $\tilde{\mathbf{W}}^-(t)$ are disturbed by two mean-zero additive noises, denoted by $\eta^+_{nm}(t)$ and $\eta^-_{nm}(t)$, and characterized by the same variance σ^2. The signals of the acquisition matrix $\tilde{\mathbf{W}}^{\pm}(t) = \tilde{\mathbf{W}}^+(t) - \tilde{\mathbf{W}}^-(t)$ in (9) are written as

$$\tilde{W}^{\pm}_{nm}(t) = W^{\pm}_{nm}(t) + \eta^{\pm}_{nm}(t) \tag{16}$$

where $\eta^{\pm}_{nm}(t) = \eta^+_{nm}(t) - \eta^-_{nm}(t)$. The two noise components $\eta^+_{nm}(t)$ and $\eta^-_{nm}(t)$ are assumed to be uncorrelated, so that the variance of $\eta^{\pm}_{nm}(t)$ is $2\sigma^2$. The decoding operation in (9) applied to (16) leads to

$$\tilde{K}^{\pm}_{nm}(t) = K^{\pm}_{nm}(t) + \zeta^{\pm}_{nm}(t) \tag{17}$$

where the variance of $\zeta^{\pm}_{nm}(t)$ is

$$\left\langle \left|\zeta^{\pm}_{nm}(t)\right|^2 \right\rangle = \left\langle \frac{1}{N^2}\sum_{p=1}^{N} \left|\eta^+_{nm}(t) - \eta^-_{nm}(t)\right|^2 H^2_{pm} \right\rangle. \tag{18}$$

Under the assumption that $\eta^+_{nm}(t)$ and $\eta^-_{nm}(t)$ are independent random variables, (18) becomes

$$\left\langle \left|\zeta^{\pm}_{nm}(t)\right|^2 \right\rangle = 2\sigma^2/N. \tag{19}$$

As previously, the standard deviation of the noise in the decoded matrix $\tilde{\mathbf{K}}^{\pm}(t)$ is divided by $N^{1/2}$ compared with the noise contained in the acquisition matrix $\tilde{\mathbf{W}}^{\pm}(t)$. However, compared with the matrix $\tilde{\mathbf{K}}(t)$ obtained without coding, the noise level is divided by a smaller factor of $\sqrt{N/2}$ because around 50% of the array elements are excited to record $\tilde{\mathbf{W}}^+(t)$ and $\tilde{\mathbf{W}}^-(t)$. Finally, the expected image quality improvement with $\tilde{\mathbf{K}}^{\pm}(t)$ corresponds to a multiplication of the SNR by a factor of $\sqrt{N/2}$.

In the third coding method where only the excitation matrix $\mathbf{H}^+_N$ is used, the noisy components of $\mathbf{W}^+_1(t) = 2\mathbf{W}^+(t) - \mathbf{P}^+(t)$ in (10) are written as

$$\left[\tilde{\mathbf{W}}^+_1\right]_{nm}(t) = \left[\mathbf{W}^+_1\right]_{nm}(t) + \eta'_{nm}(t) \tag{20}$$

where $\eta'_{nm}(t) = 2\eta^+_{nm}(t) - \eta^+_{n1}(t)$. After decoding, the components of the impulse response matrix $\tilde{\mathbf{K}}^+(t)$ are expressed as

$$\tilde{K}^+_{nm}(t) = K^+_{nm}(t) + \zeta^+_{nm}(t). \tag{21}$$

Using the following property of the Hadamard matrix:

$$\frac{1}{N}\sum_{p=1}^{N} H_{pm} = \begin{cases} 1, & \text{if } m = 1 \\ 0, & \text{if } 2 \le m \le N \end{cases} \tag{22}$$

the noise term $\zeta^+_{nm}(t)$ in (21) can be decomposed as follows:

$$\zeta^+_{nm}(t) = \begin{cases} \dfrac{2}{N}\displaystyle\sum_{p=1}^{N} \eta^+_{np}(t) H_{pm} - \eta^+_{n1}(t), & \text{if } m = 1 \\ \dfrac{2}{N}\displaystyle\sum_{p=1}^{N} \eta^+_{np}(t) H_{pm}, & \text{if } 2 \le m \le N. \end{cases} \tag{23}$$

With this decomposition, it is easy to demonstrate that the noise variance is

$$\left\langle \left|\zeta^+_{nm}(t)\right|^2 \right\rangle = \begin{cases} \sigma^2, & \text{if } m = 1 \\ 4\sigma^2/N, & \text{if } 2 \le m \le N. \end{cases} \tag{24}$$

This result shows that the noise variance is σ^2 for the N signals of the first column of the decoded matrix $\tilde{K}^+(t)$, and $4\sigma^2/N$ for the other $N^2 - N$ signals. As the final TFM image

TABLE I
THEORETICAL SNR FOR IMPULSE RESPONSE MATRICES RECORDED WITH CODED EXCITATIONS

Impulse response matrices	$\mathbf{K}(t)$	$\mathbf{K}^{+}(t)$	$\mathbf{K}^{\pm}(t)$	$\mathbf{K}^{H}(t)$
Theoretical SNR	A (ref.)	$A\sqrt{N/5}$	$A\sqrt{N/2}$	$A\sqrt{N}$

is the sum of all the components of this matrix at every point, we can express the overall noise variance $\bar{\sigma}^2$ as

$$\bar{\sigma}^2 = \sum_{n=1}^{N} \left\langle \left|\zeta_{n1}^{+}(t)\right|^2 \right\rangle + \sum_{n=1}^{N}\sum_{m=2}^{N} \left\langle \left|\zeta_{nm}^{+}(t)\right|^2 \right\rangle \tag{25}$$

which gives $\bar{\sigma}^2 = (5N-4)\sigma^2$. The noise variance for the TFM image calculated with $\tilde{\mathbf{K}}(t)$ is $N^2\sigma^2$. It follows that the coding with the excitation matrix $\mathbf{H}_N^{+}$ increases the SNR by a factor of $N/(5N-4)^{1/2}$. For arrays with large values of N, the increase in SNR can be approximated by the factor $\sqrt{N/5}$.

To summarize this theoretical analysis of the noise, the SNR expressions are given in Table I for the four impulse response matrices: $\mathbf{K}(t)$ recorded with a standard acquisition where elements are excited one by one, $\mathbf{K}^{+}(t)$ obtained with the single sparse matrix $\mathbf{H}_N^{+}$, $\mathbf{K}^{\pm}(t)$ obtained with the two sparse matrices $\mathbf{H}_N^{+}$ and $\mathbf{H}_N^{-}$, and $\mathbf{K}^{H}(t)$ recorded with the Hadamard matrix $\mathbf{H}_N$. The SNRs are given in a linear scale, and written as a function of the number of elements N and the reference SNR value A, measured with the matrix $\mathbf{K}(t)$. For clarity, the symbol "$\sim$" that designates the matrices with noise has been removed.

IV. IMAGING IN THE HDPE BASE MATERIAL

To validate the theoretical SNRs mentioned above, the TFM images are calculated in the base material of a polyethylene sample with a contact array. The experimental setup is described, as well as the characterization method to measure the phase velocity and the attenuation of bulk waves. Then, the SNRs are measured on images and compared with the theory. Finally, the DORT filtering method is combined with the Hadamard coded excitations to remove the noise in data as much as possible.

A. Experimental Setup and Material Characterization

A series of experiments was conducted to image a 1-mm-diameter side-drilled hole in the base material of an HDPE pipe (i.e., outside the fusion weld). The experimental setup is schematized in Fig. 1. The probe is a contact linear array of 64 elements manufactured by Imasonic (Voray-sur-l'Ognon, France). The pitch is 0.6 mm and the element width is $a = 0.5$ mm. The 64 elements operate around the mean center frequency $f_c = 5$ MHz with a -6 dB fractional bandwidth of 80%. The probe was fixed to the pipe above the artificial defect located at 25 mm depth, and signals were recorded with a MultiX++ system (M2M, Les Ulis, France).

The material density is $\rho = 0.95$ g/cm^3. The phase velocity $c(f)$ and the attenuation coefficient $\alpha(f)$ of the longitudinal waves were measured at 20 °C with a broadband pulse technique and a conventional immersion transmission setup composed of two single-element probes [26]. The distance between the transmitter and the receiver is $2F$, where F is the Fresnel distance. A first reference measurement $s_0(t)$ was carried in the absence of sample. The second signal $s(t)$ was recorded by introducing an HDPE plate of thickness d halfway between both transducers. Then, $c(f)$ and $\alpha(f)$ are determined by comparing the phases and amplitudes of the Fourier spectra $S_0(f)$ and $S(f)$. The phase velocity expression is

$$c(f) = \frac{2\pi f d c_0}{2\pi f d + c_0 \arg\left(\frac{S_0(f)}{S(f)}\right)} \tag{26}$$

where $c_0 = 1.483$ mm/μs is the celerity in water. The attenuation coefficient (in mm^{-1}) is given by

$$\alpha(f) = \frac{\log T + \log\left(|S_0(f)|\right) - \log(|S(f)|)}{d} + \alpha_0(f) \tag{27}$$

with

$$T = \frac{4Z_0 Z}{(Z_0+Z)^2}. \tag{28}$$

α_0 is the wave attenuation in water, which is negligible compared with that in the material. Z_0 and Z are the acoustic impedances of water and the sample.

The dispersion and attenuation curves are shown in Fig. 2 and are in good agreement with the measurements published by Lingevitch *et al.* [14]. Let us note that, in our experiment, two plates with different thicknesses were tested to plot each curve: a plate with a small thickness of $d = 4$ mm for the high frequency range [2.5–6 MHz], and a thicker plate with $d = 35$ mm for the low frequency range [1–2.5 MHz] to avoid thickness resonances.

B. TFM Images Obtained With Different Coded Excitations

The three experimental TFM images shown in Fig. 3(a)–(c) are calculated by processing with (5) the signals of the matrices $\mathbf{K}(t)$, $\mathbf{K}^{+}(t)$, and $\mathbf{K}^{\pm}(t)$. The fourth image in Fig. 3(d) was calculated with the plane wave imaging (PWI) method [27], because the Hadamard coding based on $+1/-1$ coefficients was incompatible with the multichannel acquisition system. However, the PWI image is equivalent in terms of SNR and can be interpreted in the same way, because the number of transmissions is identical (64 plane waves transmitted in the angular range from $-31.5°$ to $31.5°$ with a regular angular step) and the acquisition parameters are unchanged (same sampling frequency, preamplification gain, and excitation voltage).

In order to reinforce the experimental results, the acquisition matrices $\mathbf{K}(t)$, $\mathbf{W}^{+}(t)$, $\mathbf{W}^{-}(t)$, and $\mathbf{W}(t)$ were simulated with the CIVA software platform (CEA, LIST, Gif-sur-Yvette, France) [28], [29]. The noise-free signals were calculated with CIVA considering the experimental velocity and attenuation values. After that, a zero-mean white Gaussian noise was synthetized and adjusted so that the SNR is identical in the experimental and simulated matrices $\mathbf{K}(t)$. Finally, the same synthetized electronic noise was added to the simulated signals contained in $\mathbf{W}^{+}(t)$, $\mathbf{W}^{-}(t)$, and $\mathbf{W}(t)$, before calculating the

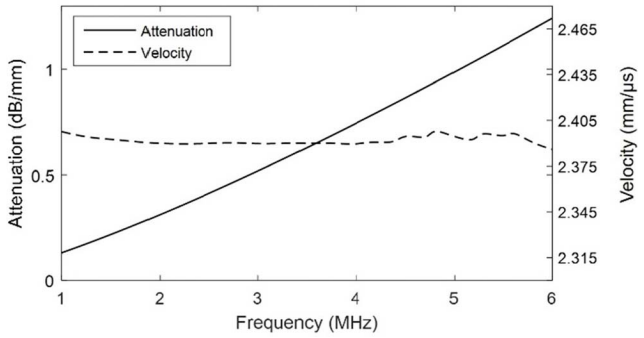

Fig. 2. Ultrasonic characterization of the HDPE material with the Sachse and Pao technique. Phase velocity $c(f)$ and attenuation $\alpha(f)$ of longitudinal bulk waves propagating in the material at 20 °C.

decoded matrices $\mathbf{K}^{+}(t)$, $\mathbf{K}^{\pm}(t)$, $\mathbf{K}^{H}(t)$, and the corresponding TFM images. The four images calculated from simulated signals are given in Fig. 3(e)–(h).

To quantify the image quality improvement, the following SNR definition has been considered:

$$\mathrm{SNR}_{\mathrm{dB}} = 20\log_{10}\frac{I_{\max}}{\sqrt{\langle I^2_{\mathrm{noise}}(\mathbf{r})\rangle}} \tag{29}$$

where $I_{\max}$ is the maximum amplitude of the defect echo, and $\langle I^2_{\mathrm{noise}}(\mathbf{r})\rangle$ is the noise variance without defect echo. According to the theoretical evolution given in Table I, the SNR in TFM imaging should be multiplied by $8/\sqrt{5}$, $4\sqrt{2}$, and 8, since the number of elements is $N = 64$. This corresponds to an increase of 11, 15, and 18 dB. With the definition (29), the reference SNR measured in Fig. 3(a) and (e) is $A = 9$ dB. Experimentally, the increase in SNR is 11 dB [Fig. 3(f)], 15 dB [Fig. 3(g)], and 19 dB [Fig. 3(h)] for the TFM images obtained from $\mathbf{K}^{+}(t)$ and $\mathbf{K}^{\pm}(t)$, and for PWI, which is in excellent agreement with the theoretical values. With simulated data, the SNR is increased by 11 dB [Fig. 3(b)], 15 dB [Fig. 3(c)], and 18 dB [Fig. 3(d)] for the images calculated with the $\mathbf{K}^{+}(t)$, $\mathbf{K}^{\pm}(t)$, and $\mathbf{K}^{H}(t)$. Thus, the simulated and experimental results shown in Fig. 3 confirm the theoretical increase in SNR according to the array excitation method. In the following, the method based on two sparse matrices will be preferred, because the SNR improvement is the most significant, and the data matrix $\mathbf{K}^{\pm}(t)$ is compatible with the noise filtering based on the DORT method. For clarity, this matrix will be denoted by $\mathbf{K}^{H}(t)$ in the following.

C. Noise Identification With the Random Matrix Theory

The singular value index $P(f)$ in (4) that separates the signal and noise subspaces at a frequency f can be determined thanks to the random matrix theory applied to a white Gaussian noise. Assuming that all the components of the noise matrix $\boldsymbol{\eta}(f)$ in (3) are independent random variables, the theory states that the density probability function of the singular values obeys to the quarter circle law [16]

$$\psi(\lambda) = \frac{1}{\pi}\sqrt{4-\lambda^2}\,\Pi_{[0;2]}(\lambda) \tag{30}$$

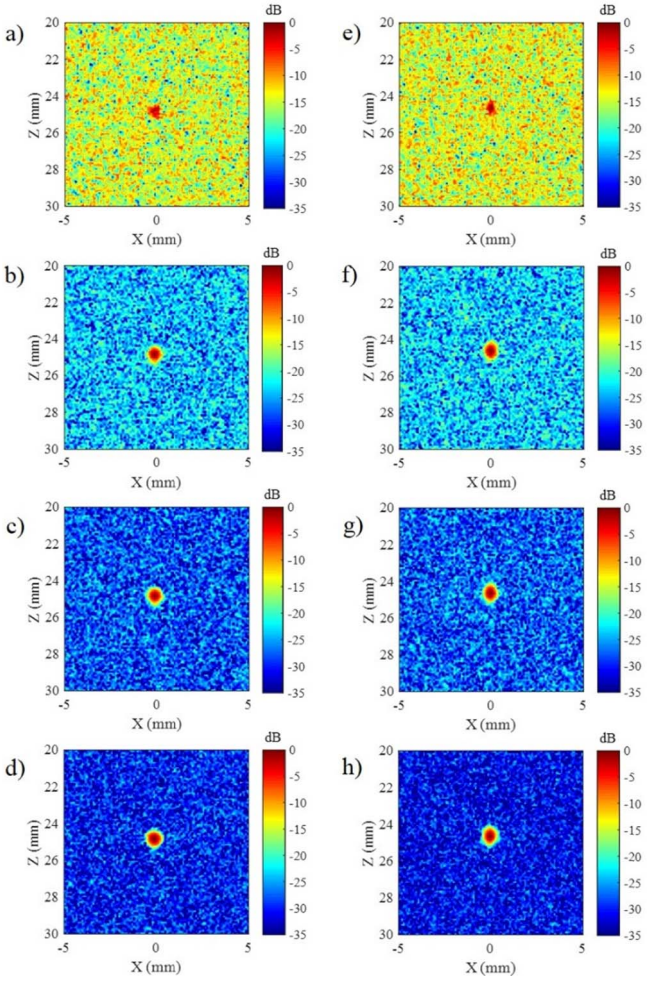

Fig. 3. TFM imaging of a side-drilled hole in a polyethylene specimen. Experimental images obtained from the data matrices (a) $\mathbf{K}(t)$, (b) $\mathbf{K}^{+}(t)$, (c) $\mathbf{K}^{\pm}(t)$, and (d) PWI image by transmitting 64 plane waves from −31.5° to 31.5°. Images calculated from the simulated data matrices (e) $\mathbf{K}(t)$, (f) $\mathbf{K}^{+}(t)$, (g) $\mathbf{K}^{\pm}(t)$, and (h) $\mathbf{K}^{H}(t)$.

where $\Pi[0; 2]$ denotes the rectangular function, i.e., $\psi(\lambda) = 0$ if $\lambda \geq 2$. Using (30), it is possible to obtain the expression of the cumulative distribution function $\Psi(\lambda) = \int_0^{\sigma} \psi(\xi)d\xi$

$$\Psi(\lambda) = \frac{1}{\pi}\left[\frac{\lambda}{2}\sqrt{4-\lambda^2} + 2\arcsin\left(\frac{\lambda}{2}\right)\right]\Pi_{[0;2]}. \tag{31}$$

As the latter function is continuous and strictly monotonically increasing, the value λ satisfies

$$\lambda = \Psi^{-1}(q) \tag{32}$$

where $0 \leq q \leq 1$, i.e., q lies in the range of $\Psi(\lambda)$. The inverse function of Ψ, as defined in (31), does not have a closed-form solution, so that Ψ^{-1} has to be computed numerically. Assuming that the rank of the filtered matrix $\hat{\mathbf{K}}_s^{H}(f)$ is $P(f)$, then the theoretical noise singular values λ_p^{th} for $1 + P(f) \leq p \leq N$, and ordered in decreasing order, can be written by

$$\lambda_p^{\mathrm{th}}(P(f)) = \Psi^{-1}\left(\frac{N-p}{N-P(f)-1}\right). \tag{33}$$

To determine $P(f)$, we consider the vector $\mathbf{s}_n(f)$ that contains the last $N-n$ experimental singular values calculated by SVD,

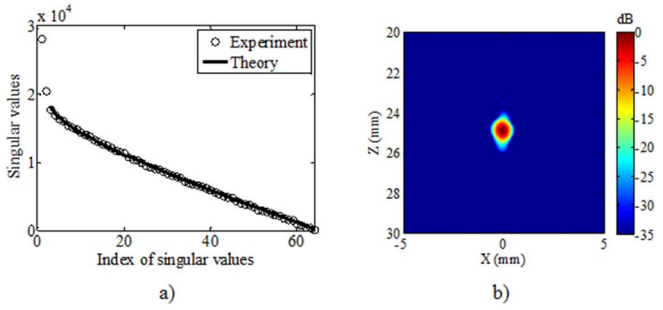

Fig. 4. (a) Comparison of the theoretical noise singular values with the experimental ones calculated at 5 MHz. (b) TFM image with the modified Hadamard codes and the noise filtering operation based on the DORT method.

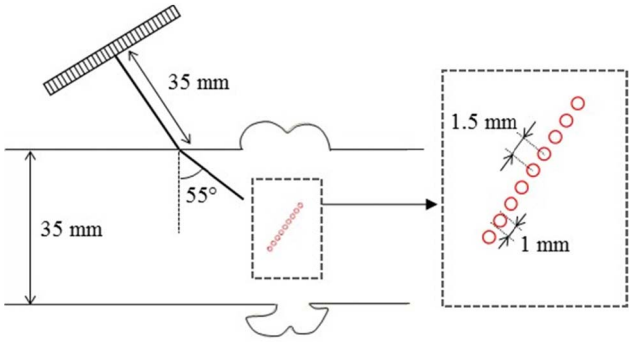

Fig. 5. Immersion testing configuration for the HDPE fusion weld. The array probe is inclined in water to 1-mm-diameter to image holes in the complex weld with a refraction angle of 55°.

and a theoretical vector of the same size as $\mathbf{s}_n(f)$

$$\mathbf{b}_n(f) = \left(\lambda_{n+1}^{\text{th}}(P(f)) \cdots \lambda_N^{\text{th}}(P(f))\right)^t. \tag{34}$$

The maximum of the cross correlation between the two vectors leads to the value of $P(f)$

$$P(f) = \left(\arg\max_n(\langle \mathbf{s}_n(f), \mathbf{b}_n(f)\rangle)\right). \tag{35}$$

The experimental singular values resulting from the decomposition of $\hat{\mathbf{K}}^H(f)$ at 5 MHz are given in Fig. 4(a). Using (34), it was determined that, at this frequency, the two singular values belong to the signal subspace. It can be observed that the theoretical curve of the noise singular values correctly fits the experimental values. The signal subspace determination consists in identifying the values that do not belong to the theoretical decay curve of the noise singular values for all the frequencies. Next, a new transfer matrix $\hat{\mathbf{K}}_s^H(f)$ is built with (4) and, after an inverse Fourier transform, the TFM algorithm can be applied to the noise-free impulse response matrix $\mathbf{K}_s^H(t)$ that provides an image with a low noise level. The SNR measured in Fig. 4(b) is 53 dB, which corresponds to an increase of 44 dB in comparison with the TFM image in Fig. 3(e). It should be noted that coded transmissions are necessary for the noise filtering method to be effective. At a depth of 25 mm in polyethylene, the SVD of the conventional transfer matrix $\hat{\mathbf{K}}(f)$ shows that there are too few frequencies in the transducer bandwidth where the signal subspace can be clearly identified, so that the filtered TFM image is not better than that given in Fig. 3(a).

V. Application to Flaw Imaging in a Weld

The TFM imaging combined with the spatial coding and the DORT method was evaluated with the immersion testing configuration presented in Fig. 5. The array characteristics are the same as in the previous experiments. The HDPE specimen under testing comprises a fusion weld with a complex geometry. A series of nine identical and parallel holes of 1 mm diameter is aligned and regularly spaced in the weld with a center-to-center distance of 1.5 mm. In order to overcome the problem related to the weld surface, the array probe was moved away from the weld and inclined above the plane surface of the base material. The inclination angle ensures a maximum insonification around 55° in the material,

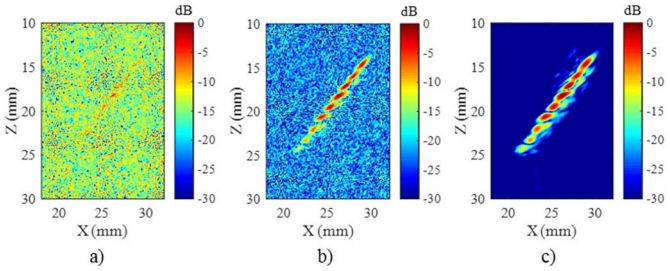

Fig. 6. Experimental TFM images of artificial flaws in an HDPE fusion weld. (a) Image with the conventional impulse response matrix $\mathbf{K}(t)$. (b) Image with the decoded matrix $\mathbf{K}^H(t)$. (c) Image with $\mathbf{K}_s^H(t)$, where the noise is filtered with the DORT method.

i.e., toward the region of interest. The TFM images are calculated with (5), where the theoretical times of flight $t_{nm}(\mathbf{r})$ through the water/solid interface are determined with a ray-based forward model and an iterative numerical method [27]. Compared to the experiments with a contact array, here no apodization is used because this would complicate the definition of the weighting coefficients (7), and would increase significantly the computation times without bringing noticeable changes in the final image.

Before the TFM image formation, a $[3.5 - 10]$ MHz bandpass filter was applied to the acquired data in order to remove the low frequencies, and thus to maximize the frequency response of the defects around 5 MHz. Without this prior filtering, the frequency response is centered at 2 MHz due to the strong attenuation, and the spatial resolution does not allow to separate the defect echoes. A probe operating around 2 MHz would be sufficient for detection, but not for characterization.

Three images of the flaws are given in Fig. 6. The first one in Fig. 6(a) was obtained with a conventional acquisition of the impulse response matrix $\mathbf{K}(t)$ and without filtering. The signal level is so low that the SNR cannot be properly measured. The improvement observed in Fig. 6(b) is due solely to the coded transmissions with the matrices $\mathbf{H}_N^+$ and $\mathbf{H}_N^-$. The SNR is 20 dB without additional processing in the frequency domain. The third TFM image in Fig. 6(c) was calculated with the same matrix $\mathbf{K}^H(t)$ and by filtering the residual noise with the DORT method. Compared with the first image,

the image quality improvement is dramatic, since the SNR reaches 40 dB.

VI. Conclusion

In this paper, spatial Hadamard codes are proposed to obtain an equivalent impulse response matrix that facilitates the noise filtering with the DORT method. The signal and noise subspaces are clearly identified at each frequency thanks to a model that predicts the singular values associated with electronic noise. After the filtering procedure, the TFM imaging applied to the data allows to image point-like defects with a high SNR and optimal resolution at 5 MHz in the butt fusion weld of an HDPE pipe.

Future works will focus on the detection of defects close to the inner surface of the pipe, such as crack-type defects. Additional experiments will also be conducted with other materials where the low SNR is a limiting factor, like carbon/epoxy composites, titanium alloys, or nuclear coarse-grained steels.

Acknowledgment

The authors would like to thank G. Daniel from the CEA, LIST for his help in the experimental setups, and the M2M Company for the provision of the polyethylene samples.

References

[1] J. S. Egerton, M. J. S. Lowe, H. V. Halai, and P. Huthwaite, "Improved FE simulation of ultrasound in plastics," in *Proc. AIP Conf.*, vol. 1706. 2016, p. 120001.

[2] L. Piche, "Phenomena related to the propagation of ultrasound in polymers (a paradigm for disordered materials)," in *Proc. IEEE Ultrason. Symp.*, Oct. 1989, pp. 599–608.

[3] M. Troughton, M. Spicer, and F. Hagglund, "Development of ultrasonic phased array inspection of polyethylene pipe joints," in *Proc. PVP Pressure Vessel Piping Conf.*, Toronto, ON, Canada, Jul. 2012, pp. 285–293.

[4] J. A. Jensen, S. I. Nikolov, K. L. Gammelmark, and M. H. Pedersen, "Synthetic aperture ultrasound imaging," *Ultrasonics*, vol. 44, pp. 5–15, Dec. 2006.

[5] A. J. Hunter, B. W. Drinkwater, and P. D. Wilcox, "The wavenumber algorithm for full-matrix imaging using an ultrasonic array," *IEEE Trans. Ultrason., Ferroelect., Freq. Control*, vol. 55, no. 11, pp. 2450–2462, Nov. 2008.

[6] C. Prada, S. Manneville, D. Spoliansky, and M. Fink, "Decomposition of the time reversal operator: Detection and selective focusing on two scatterers," *J. Acoust. Soc. Amer.*, vol. 99, no. 4, pp. 2067–2076, 1996.

[7] E. L. Villaverde, S. Robert, and C. Prada, "Ultrasonic imaging of defects in coarse-grained steels with the decomposition of the time reversal operator," *J. Acoust. Soc. Amer.*, vol. 140, no. 1, pp. 541–550, 2016.

[8] K. L. Gammelmark and J. A. Jensen, "Multielement synthetic transmit aperture imaging using temporal encoding," *IEEE Trans. Med. Imag.*, vol. 22, no. 4, pp. 552–563, Apr. 2003.

[9] R. Y. Chiao and L. J. Thomas, "Synthetic transmit aperture imaging using orthogonal Golay coded excitation," in *Proc. IEEE Ultrason. Symp.*, Oct. 2000, pp. 1677–1680.

[10] M. Karaman, P.-C. Li, and M. O'Donnell, "Synthetic aperture imaging for small scale systems," *IEEE Trans. Ultrason., Ferroelect., Freq. Control*, vol. 42, no. 3, pp. 442–449, May 1995.

[11] S. Bannouf, S. Robert, and C. Prada, "Data set reduction for ultrasonic TFM imaging using the effective aperture approach and virtual sources," in *Proc. J. Phys. Conf. Ser.*, vol. 457. 2013, p. 012007.

[12] S. D. Silverstein, "Application of orthogonal codes to the calibration of active phased array antennas for communication Satellites," *IEEE Trans. Signal Process.*, vol. 45, no. 1, pp. 206–218, Jan. 1997.

[13] R. Y. Chiao, L. J. Thomas, and S. D. Silverstein, "Sparse array imaging with spatially-encoded transmits," in *Proc. IEEE Ultrason. Symp.*, Oct. 1997, pp. 1679–1682.

[14] J. F. Lingevitch, H. C. Song, and W. A. Kuperman, "Time reversed reverberation focusing in a waveguide," *J. Acoust. Soc. Amer.*, vol. 111, no. 6, pp. 2609–26014, 2002.

[15] P. Nauleau *et al.*, "A method for the measurement of dispersion curves of circumferential guided waves radiating from curved shells: Experimental validation and application to a femoral neck mimicking phantom," *Phys. Med. Biol.*, vol. 61, no. 13, pp. 4746–4762, 2016.

[16] V. A. Marčenko and L. A. Pastur, "Distribution of eigenvalues for some sets of random matrices," *Math. USSR-Sbornik*, vol. 1, no. 4, pp. 457–483, 1967.

[17] J. Seberry and M. Yamada, "Hadamard matrices, sequences and block designs," *Contemporary Design Theory—A Collection of Surveys*. 1992, pp. 431–560.

[18] E. Iakovleva, S. Chatillon, P. Bredif, and S. Mahaut, "Multi-mode TFM imaging with artifacts filtering using CIVA UT forwards models," in *Proc. AIP Conf.*, vol. 1581. 2014, p. 72.

[19] A. Selfridge, G. S. Kino, and B. Khuri-Yakub, "A theory for the radiation pattern of a narrow strip acoustic transducer," *Appl. Phys. Lett.*, vol. 37, no. 35, pp. 35–36, 1980.

[20] C. Fan, M. Caleap, M. Pan, and B. W. Drinkwater, "A comparison between ultrasonic array beamforming and super resolution imaging algorithms for non-destructive evaluation," *Ultrason.*, vol. 54, no. 7, pp. 1842–1850, 2014.

[21] J. Wu, "Determination of velocity and attenuation of shear waves using ultrasonic spectroscopy," *J. Acoust. Soc. Amer.*, vol. 99, no. 5, pp. 2871–2875, 1996.

[22] S. Robert, F. Cartier, L. de Roumilly, R.-O. Mondou, P.-E. Lhuillier, and G. Garzino, "Adaptive ultrasonic imaging with a phased-array probe equipped with a conformable wedge," in *Proc. 19th World Conf. Non-Destruct. Testing*, Munich, Germany, Jun. 2016, pp. 13–16.

[23] T. Harrison, A. Sampaleanu, and R. Zemp, "S-sequence spatially-encoded synthetic aperture ultrasound imaging," *IEEE Trans. Ultrason., Ferroelect., Freq. Control*, vol. 61, no. 5, pp. 886–890, May 2014.

[24] P. Gong, M. C. Kolios, and Y. Xu, "Delay-encoded transmission and image reconstruction method in synthetic transmit aperture imaging," *IEEE Trans. Ultrason., Ferroelect., Freq. Control*, vol. 62, no. 10, pp. 1745–1756, Oct. 2015.

[25] E. L. Villaverde, S. Robert, and C. Prada, "Ultrasonic imaging in highly attenuating materials with Walsh–Hadamard codes and the decomposition of the time reversal operator," in *Proc. IEEE Int. Ultrason. Symp.*, Sep. 2016, pp. 1–4.

[26] W. Sachse and Y.-H. Pao, "On the determination of phase and group velocities of dispersive waves in solids," *J. Appl. Phys.*, vol. 49, no. 8, p. 4320, 1978.

[27] L. Le Jeune, S. Robert, E. L. Villaverde, and C. Prada, "Plane wave imaging for ultrasonic non-destructive testing: Generalization to multi-modal imaging," *Ultrasonics*, vol. 64, pp. 128–138, Jan. 2016.

[28] M. Darmon, N. Leymarie, S. Chatillon, and S. Mahaut, "Modelling of scattering of ultrasounds by flaws for NDT," in *Ultrasonic Wave Propagation in Non Homogeneous Media* (Springer Proceedings in Physics), vol. 128. 2013, pp. 61–71.

[29] M. Darmon and S. Chatillon, "Main features of a complete ultrasonic measurement model: Formal aspects of modeling of both transducers radiation and ultrasonic flaws responses," *Open J. Acoust.*, vol. 3, no. 3A, pp. 43–53, 2013.

Eduardo Lopez Villaverde was born in Mexico City, Mexico, in 1987. He received the B.Eng. degree in electronics from Universidad Autónoma de Baja California, Ensenada, Mexico, and the M.Eng. degree in electronics and computer science from École nationale supérieure de l'électronique et de ses applications, Cergy, France. He is currently pursuing the Ph.D. degree in physical acoustics with Universite Paris Diderot 7, Paris, France, and the Laboratory for Integration of Systems and Technology, Commissariat à l´Énergie Atomique et aux Énergies Alternatives, Department of Imaging and Simulation for Nondestructive Testing, Gif-sur-Yvette, France.

His current research interests include ultrasonic array imaging, beamforming techniques, and noise filtering in complex media.

Sébastien Robert was born in Fécamp, France, in 1975. He received the master's degree in physical acoustics and the Ph.D. degree with a focus on wave propagation in periodic and random multiple scattering media from Le Havre University, Le Havre, France, in 2001 and 2005, respectively.

He held a CNRS post-doctoral position with the Institut Langevin, Paris, France, for two years. He joined Laboratory for Integration of Systems and Technology, Commissariat à l'Énergie Atomique et aux Énergies Alternatives, Gif-sur-Yvette, France, as a Research Engineer in ultrasound imaging, where he has been a Researcher since 2009. His current research interests include multiple scattering in solids, time reversal techniques, real-time array imaging, and adaptive methods applied to complex geometries and materials.

Claire Prada was born in Paris in 1962. She studied mathematics at Ecole Normale Supérieure, Paris, France, and received the M.S. degrees in mathematics and physical acoustics from Université Pierre et Marie Curie, Paris, and the Ph.D. degree in physical acoustics from University Paris Diderot, Paris, in 1991.

She was appointed as a Research Scientist by CNRS to work in the Laboratoire Ondes et Acoustique in 1990. She is currently a Research Director of the Institut Langevin, Paris. She studies acoustic and elastic wave propagation using multielements methods and laser ultrasonic techniques. A large part of her work focused on time reversal acoustics and the related DORT method with applications in shallow water acoustics and ultrasonic imaging. She is also involved in elastic guided waves, especially on zero group velocity and backward Lamb modes, and their applications to nondestructive evaluation.